Journal of Non-Newtonian Fluid Mechanics 177–178 (2012) 89–96

Contents lists available at SciVerse ScienceDirect

Journal of Non-Newtonian Fluid Mechanics

journal homepage: http://www.elsevier.com/locate/jnnfm

Experimental evidence of the critical phenomenon and shear banding flow in polymer-like micellar solutions

F. Bautista [a,*], V.V.A. Fernández [c], E.R. Macías [b], J.H. Pérez-López [b], J.I. Escalante [b], J.E. Puig [b], O. Manero [d]

[a] Departamento de Física, Universidad de Guadalajara Boul. M. García Barragán #1451, Guadalajara, Jal. 44430, Mexico
[b] Departamento de Ingeniería Química, Universidad de Guadalajara Boul. M. García Barragán #1451, Guadalajara, Jal. 44430, Mexico
[c] Departamento de Ciencias Tecnologicas, Universidad de Guadalajara, Av. Universidad #1115, Ocotlan, Jal. 47820, Mexico
[d] Instituto de Investigaciones en Materiales, Universidad Nacional Autónoma de México, Apdo. Postal 70-360, México DF 04510, Mexico

ARTICLE INFO

Article history:
Received 13 January 2012
Received in revised form 9 March 2012
Accepted 9 March 2012
Available online 16 April 2012

Keywords:
Rheo-optics
Micellar solutions
Lyapunov exponents
Critical point
Shear-banding flow
BMP model

ABSTRACT

Steady shear and rheo-optical experimental data measured in several micellar solutions, demonstrate the existence of a non-equilibrium critical point (*necp*) in the shear banding flow of wormlike micellar solutions by the following evidence: (1) the disappearance of the coexistence of two steady banded fluids at the *necp*, (2) the curves of the reduced shear stress versus reduced shear rate become anti-symmetric in the neighborhood of the non-equilibrium critical point; (3) flow birefringence increases considerably in the neighborhood of the *necp*; (4) the divergence of non-equilibrium thermodynamic properties (isothermal flow susceptibility and the normalized heat dissipation), as the *necp* is approached; and (5) the existence of a finite correlation dimension calculated from time analysis of birefringence data, and positive Lyapunov exponents, which are consistently smaller than the embedding dimension.

The predictions of the BMP model follow these trends closely.

1. Introduction

Shear banding flow is an interesting and important manifestation of the nonlinear rheology of wormlike micelles. This flow phenomenon has been observed in many wormlike micellar systems in both the semidilute and concentrated regimes [1,2] as well as in many other complex fluids such as lamellar phases [3], associative polymer solutions [4], and bicontinuous microemulsions [5]. Hence, this flow phenomenon appears to be quite general for complex fluids. Shear banding appears as a discontinuity in the shear stress-shear rate flow curve, in which a plateau stress (σ_p) develops between two critical shear rates, $\dot{\gamma}_{c1}$ and $\dot{\gamma}_{c2}$; below and above these shear rates, the flow is homogeneous and usually Newtonian. Long transients and oscillations in rheological and optical measurements accompany this flow phenomenon [6–15]. Shear banding flow in wormlike micelles has been identified by flow birefringence [10], NMR velocimetry [9,16], small-angle light (SALS), neutron (SANS) and X-ray (SAXS) scattering techniques [17–19], particle image visualization (PIV) and particle tracking velocimetry (PTV) [19].

The most commonly invoked mechanism for shear banding is the shear-induced phase transition, especially near the isotropic–nematic phase transition, although other mechanisms such as mechanical instability have been proposed [20–24]. The arguments that support the shear-induced transition mechanism are: (1) a reversible shear-induced structural or non-equilibrium phase transition is typically observed; (2) the plateau stress is unique and robust since it is independent of shear history; (3) the long stress transients and oscillations in start-up shear flows resemble the kinetics of nucleation and growth of a second phase, similar to phenomena reported in equilibrium first-order phase transitions; and (4) the generalized *master flow-phase diagram*, obtained by applying a temperature–concentration superposition, is remarkably similar to equilibrium liquid–vapor phase diagrams [2,25,26]. Most details of shear-induced structural changes in wide concentration ranges and the underlying associated mechanisms are still open questions.

Several model approaches have been forwarded to explain the non-equilibrium phase transition mechanism. One of the first theories for polymers was proposed by McLeish and Ball [27]. Relevant shear-flow effects on critical fluctuations in a binary fluid that possesses an equilibrium critical point have been discussed by Onuki and Kawasaki [28]; in this case, shear flow suppresses fluctuations. The connection between extensional flow and phase transitions in nematic systems has been discussed by several authors [29–31]. Nematic systems under shear flow provide examples of phase transitions under non-equilibrium conditions; here the equilibrium isotropic–nematic transition is first order, and

* Corresponding author.
E-mail address: ferbautistay@yahoo.com (F. Bautista).

0377-0257/$ - see front matter © 2012 Published by Elsevier B.V.
http://dx.doi.org/10.1016/j.jnnfm.2012.03.006

Nomenclature

σ	shear stress
σ_p	stress plateau
$\dot{\gamma}_{c1}$	first critical shear rates (rate at which the stress plateau begins)
$\dot{\gamma}_{c2}$	second critical shear rates (rate at which the stress plateau ends)
$\dot{\gamma}$	shear rate
φ	fluidity (inverse of the shear viscosity (η))
φ_0	fluidity at zero shear rate
φ_∞	fluidity at infinite shear rate
λ	structure relaxation time
k_0	structure breaking constant
ϑ	shear banding intensity parameter
G_0	plateau modulus
τ_R	main relaxation time
Σ	dimensionless shear stress
$\dot{\Gamma}$	dimensionless shear rate
$\dot{\Gamma}_{c1}$	dimensionless first critical shear rate
$\dot{\Gamma}_{c2}$	dimensionless second critical shear rate
$\mathbf{\Phi}$	dimensionless fluidity
$\boldsymbol{\lambda}$	dimensionless structure relaxation time
k	dimensionless structure breaking constant
ϑ	dimensionless shear banding intensity parameter
$\boldsymbol{\varphi}_\infty$	dimensionless fluidity at infinite shear rate
Σ_c	shear stress at the non-equilibrium critical point
$\dot{\Gamma}_c$	shear rate at the non-equilibrium critical point
$\mathbf{\Phi}_c$	fluidity at the non-equilibrium critical point
ϑ_c	shear banding intensity parameter at the non-equilibrium critical point
Σ_r	reduced shear stress
$\dot{\Gamma}_r$	reduced shear rate
$\mathbf{\Phi}_r$	reduced fluidity
necp	non-equilibrium critical point
$\Delta n'$	birefringence
ξ	variance of the birefringence
$\mathcal{G}$	dissipated energy
$\widehat{\mathcal{G}}$	normalized dissipated energy
κ_T	isothermal flow susceptibility
C_σ	normalized power dissipation under shear banding flow
$\bar{\mathrm{J}}$	mass flux vector
$\underline{\underline{\sigma}}$	stress tensor
$\underline{\underline{L}}$	velocity gradient tensor
$\underline{\underline{D}}$	symmetric part of rate of strain tensor
II_D	second invariant
τ_1	relaxation time for the mass flux
$\mathcal{D}$	Fickean diffusion coefficient
C	local equilibrium concentration
β_0, β_0', β_2 and β_2'	are phenomenological parameters

the suppression of orientation fluctuations by shear flow makes possible a non-equilibrium critical point (*necp*) associated with amplitude fluctuations. Attention to non-equilibrium phase diagrams spanned by temperature and shear rate in nematic liquid crystals has been given attention by Olmsted and Goldbart [32,33]. On the experimental side, the analog between the thermodynamic and banding spinodals has been inferred by Berret and Porte [15].

Recently, we derived the generalized Bautista–Manero–Puig (BMP) model from the coupling of flow and concentration using an extended irreversible thermodynamic approach [34]. This model predicts the existence of a non-equilibrium critical point (*necp*) that occurs when the shear banding region vanishes; we were able to obtain the non-equilibrium critical exponents and showed that they are non-classic but they follow the Widom's inequality [35].

Here we present steady shear data for several aqueous micellar solutions, in which temperature, surfactant concentration or surfactant/salt ratio is varied. Rheological data indicate that regardless of the varying parameter, the shear-banding region shrinks up to a non-equilibrium critical point, at which shear-banding flow vanishes. Above this point, only homogeneous Newtonian flow is detected. In the neighborhood of the *necp*, the curves of the reduced shear stress versus reduced shear rate become antisymmetric, similar to the ferromagnetic critical transition [36]. Moreover, rheo-optical measurements show that the variance of flow birefringence becomes more intense and erratic as the *necp* is approached and becomes less intense and more regular far below or above this point. The experimental data demonstrate that the isothermal flow susceptibility (analogous to the isothermal compressibility) and the normalized power dissipation (analogous of the heat capacity) diverge as the *necp* is approached. This model predicts remarkably well experimental data and shows that the two minima in the dissipated free energy-versus-reduced shear rate (which indicate the position of the critical shear rates that limit the shear banding region), approach each other, become shallower and eventually disappear at the *necp* to produce a flat profile.

2. The model

We have pointed out in a previous paper [34] that the derivation from irreversible thermodynamics leads to three coupled equations: the constitutive equation for the stress, the equation for the diffusion of mass and the equation for the rate of change of the microstructure due to the flow. The relevant equations of the 3- D BMP model are:

$$\frac{d\varphi}{dt} = \frac{1}{\lambda}(\varphi_0 - \varphi) + k_0(1 + \vartheta II_D)(\varphi_\infty - \varphi)\underline{\underline{\sigma}} : \underline{\underline{D}} + \varphi_0\beta_0'\nabla\cdot\bar{\mathrm{J}}, \tag{1}$$

$$\bar{\mathrm{J}} + \tau_1\frac{\varphi_0}{\varphi}\overset{\nabla}{\bar{\mathrm{J}}} = -\frac{\mathcal{D}\varphi_0}{\varphi}\nabla c - \frac{\beta_0}{\varphi}\nabla\varphi + \frac{\beta_2\varphi_0}{\varphi}\nabla\cdot\underline{\underline{\sigma}}, \tag{2}$$

$$\underline{\underline{\sigma}} + \frac{1}{G_0\varphi}\overset{\nabla}{\underline{\underline{\sigma}}} = \frac{2}{\varphi}\underline{\underline{D}} + \frac{\beta_2'\varphi_0}{\varphi}\nabla\bar{\mathrm{J}}. \tag{3}$$

where the upper-convected derivatives of the mass flux vector $\bar{\mathrm{J}}$ and of the stress tensor $\underline{\underline{\sigma}}$ are defined, respectively, as:

$$\overset{\nabla}{\bar{\mathrm{J}}} = \frac{\mathrm{d}\bar{\mathrm{J}}}{\mathrm{dt}} - \underline{\underline{\mathrm{L}}}\cdot\bar{\mathrm{J}}, \tag{4}$$

$$\overset{\nabla}{\underline{\underline{\sigma}}} = \frac{\mathrm{d}\underline{\underline{\sigma}}}{\mathrm{dt}} - \left(\underline{\underline{\mathrm{L}}}\cdot\underline{\underline{\sigma}} + \underline{\underline{\sigma}}\cdot\underline{\underline{\mathrm{L}}}^T\right). \tag{5}$$

Here $\underline{\underline{\mathrm{L}}}$ is the velocity gradient tensor, $\underline{\underline{D}}$ is the symmetric part of rate of strain tensor and II_D is its second invariant, φ is the inverse of the shear viscosity (η) or fluidity, $\varphi_0(\equiv\eta_0^{-1})$ is the fluidity at zero shear rate, G_0 is the plateau shear modulus, λ is a structure relaxation time, k_0 can be interpreted as a kinetic parameter for structure breaking in the absence of shear flow, ϑ is the shear banding intensity parameter, τ_1 is a relaxation time for the mass flux, D is the Fickean diffusion coefficient, c is the local equilibrium concentration and ϑ, β_0, β_0' , β_2 and β_2' are phenomenological parameters.

For steady simple-shear, assuming that the gradients in φ and c vary along in the y-direction, and after neglecting the relaxation time for the mass flux, Eqs. (1)–(3) become:

$$\frac{1}{\lambda}(\varphi_0-\varphi)+k_0(1+\vartheta\dot{\gamma})(\varphi_\infty-\varphi)\sigma\dot{\gamma}+\varphi_0\beta_0'\frac{\partial J_y}{\partial y}=0, \tag{6}$$

$$J_x=\frac{\beta_2\varphi_0}{\varphi}\frac{\partial\sigma}{\partial y}, \tag{7a}$$

$$J_y=-\frac{\mathcal{D}\varphi_0}{\varphi}\frac{\partial c}{\partial y}-\frac{\beta_0}{\varphi}\frac{\partial\varphi}{\partial y}, \tag{7b}$$

$$\sigma=\frac{\dot{\gamma}}{\varphi}+\frac{\beta_2'\varphi_0}{\varphi}\frac{\partial J_x}{\partial y}. \tag{8}$$

We have assumed that normal stresses are negligible. Eqs. (6)–(8) embody particular cases. For instance, substituting Eq. (7b) into Eq. (6) for the case where differences in concentration are negligible yields:

$$\frac{1}{\lambda}(\varphi_0-\varphi)+\kappa_0(1+\vartheta\dot{\gamma})(\varphi_\infty-\varphi)\sigma\dot{\gamma}-\varphi_0\beta_0\beta_0'\frac{\partial}{\partial y}\left(\frac{1}{\varphi}\frac{\partial\varphi}{\partial y}\right)=0. \tag{9}$$

In addition, when Eq. (7a) is substituted in Eq. (8), gives:

$$\sigma=\frac{\dot{\gamma}}{\varphi}+\frac{\beta_2\beta_2'\varphi_0^2}{\varphi}\frac{\partial}{\partial y}\left[\frac{1}{\varphi}\frac{\partial\sigma}{\partial y}\right]. \tag{10}$$

Eqs. (9) and (10) now contain diffusion terms for the stress and for the structure, respectively. As pointed out further, a banding solution is by definition, one that has no gradients of the fluidity (representative of the current structure) at the boundaries. For the condition where the phase coexistence is present, the fluidity is constant within the bulk of each phase, and it changes suddenly at the interface. We then henceforth obtain Eqs. (9) and (10). In this sense, the model from which the critical behavior is analyzed is not rheologically simple.

As shown elsewhere [35], under steady shear flow, the model equations reduce to:

$$\frac{1}{\lambda}(\varphi_0-\varphi)+k_0(1+\vartheta\dot{\gamma})(\varphi_\infty-\varphi)\sigma\dot{\gamma}=0 \tag{11}$$

$$\sigma=\frac{\dot{\gamma}}{\varphi}. \tag{12}$$

In these equations, σ is the shear stress and $\dot{\gamma}$ is the shear rate. Normal stresses are not included in Eqs. (11) and (12), since their contribution does not change qualitatively the results, as shown elsewhere [37]. The model requires five parameters for steady shear flow: φ_0, φ_∞, λ, k_0 and ϑ, which can be obtained from single independent rheological experiments, and they are employed to predict other rheological data [6,38,39]. φ_0 and φ_∞ are obtained from steady shear measurements at low and high shear rates, respectively. However, if the shear-rate range is not high enough to reach the high-shear rate viscosity plateau, φ_∞ can be obtained by fitting the linear oscillatory viscous modulus, G", with the Hess equation, given by [40]:

$$G''=\left(\frac{\eta_0-\eta_\infty}{\tau_R}\right)\left(\frac{\omega\tau_d}{1+\omega^2\tau_d^2}\right)+\omega\eta_\infty, \tag{13}$$

where τ_d is the main relaxation time of the sample and ω is the applied frequency. λ, can be obtained from the intercept of the stress relaxation curve at long times after cessation of steady shear flow, where the intercept is given by $\exp[-G_0\lambda(\varphi_{ss}-\varphi_0)]$, being φ_{ss} the steady state fluidity prior to the cessation of shear flow, and the plateau modulus, G_0, can be obtained by oscillatory shear measurements or from instantaneous stress relaxation experiments [38]. k_0, in turn, can be evaluated by fitting numerically the stress growth coefficient, η^+, from inception of shear flow experiments [38]. Finally, if normal forces are neglected, ϑ is uniquely determined by the value of the stress at the plateau region according to [39]:

$$\Delta\mathcal{G}=\frac{\nu}{G_0\varphi_0}\int\frac{\dot{\gamma}_{12}}{\varphi}d\dot{\gamma}_{12}=0, \tag{14}$$

where $\mathcal{G}$ is the generalized Gibbs free energy or dissipated energy andφ is the solution of Eqs. (11) and (12) combined. This equation is similar to that reported by Dhont [41] when the shear curvature viscosity in Dhont's equation is independent of shear rate. In this case, the stress selection rule given by Eq. (14) implies an equal-area Maxwell construction in a $\sigma-\dot{\gamma}$ plot. Alternatively, since the dissipation energy of the bands must be equal at the stationary banding state, the criterion is the equal minima in the dissipated energy of the bands in plots of $\mathcal{G}$ versus $\dot{\gamma}$. Incidentally, we have shown elsewhere that the values of the critical shear rates and of the plateau stress are the same even when normal stresses are included in the analysis [39]. Table 1 reports the parameters of the model, the characteristics of the micellar systems employed and the references from which data were taken.

Substitution of Eq. (12) into Eq. (11) yields a dimensionless cubic equation in shear rate that can be expressed in terms of the dimensionless variables $\Sigma=\sigma/G_0$ and $\dot{\Gamma}=\dot{\gamma}\tau_R$, being G_0 the plateau modulus and τ_R the main relaxation time [25]:

$$\dot{\Gamma}^3+\left(-\varphi_\infty\Sigma+\frac{1}{\vartheta}\right)\dot{\Gamma}^2+\left(-\frac{\varphi_\infty}{\vartheta}\Sigma+\frac{1}{k\vartheta\Sigma}\right)\dot{\Gamma}-\frac{1}{k\vartheta}=0, \tag{15}$$

where $k=G_0k_0\lambda/\tau_R$, $\lambda=\lambda/\tau_R$, $\vartheta=\vartheta/\tau_R$ and $\boldsymbol{\varphi}_\infty=G_0\tau_R\varphi_\infty=\varphi_\infty/\varphi_0$.

By definition of the reduced variables, $\Sigma_r=\Sigma/\Sigma_c$, $\dot{\Gamma}_r=\dot{\Gamma}/\dot{\Gamma}_c$ and $\boldsymbol{\Phi}_r=\boldsymbol{\Phi}/\boldsymbol{\Phi}_c$ (being $\boldsymbol{\Phi}=\Sigma/\dot{\Gamma}$), where the subscript c indicates the values of these variables at *necp*, Eq. (15) becomes:

$$(\boldsymbol{\varphi}_c^{-1}-\boldsymbol{\Phi}_r)+k\dot{\Gamma}_c\Sigma_c(1+\vartheta\dot{\Gamma}_c\dot{\Gamma}_r)(\boldsymbol{\varphi}_c^{-1}\boldsymbol{\varphi}_\infty-\boldsymbol{\Phi}_r)\Sigma_r\dot{\Gamma}_r=0 \tag{16}$$

This equation suggests that only two dimensionless model parameters are independent. However, the reduced fluidity (Φ_r) is not an independent variable [35], and therefore, there is only one independent variable left in Eq. (16).

The normalization with respect critical point implies that the curve of $\sum_{\mathbf{r}}$ versus $\dot{\Gamma}_r$ is anti-symmetric, so the generalized free energy can be shown to satisfy the scaling hypothesis. Consequently, some thermodynamic properties (κ_T,$\dot{\Gamma}_{c1}-\dot{\Gamma}_{c2}$ and C_σ; see definitions in the text below) follow power law relationships and critical exponents can thus be defined.

3. Experimental section

Cetyltrimethylammonium tosylate (CTAT), 98% pure from Sigma, and dodecyltrimethylammonium bromide (DTAB), 98%+ pure from Tokyo Kasei, were further purified by re-crystallization from a chloroform–ethyl ether mixture (50:50 by volume). Sodium salycilate (NaSal) with purity larger than 99% from Fluka, and Pluronics P103 [$(EO)_{17}(PO)_{60}(EO)_{17}$] from BASF, were used as received. Water, with conductivity smaller than 6 μS/cm drawn from a Millipore purification system, was used.

CTAT and P103 samples were prepared by weighing the surfactant and the water in glass vials that were placed in a water bath at 30 °C for a week, where they were frequently shaken to speed up homogenization. Then, samples were allowed to reach equilibrium at the measurement temperature. P103 samples were covered with aluminum foil to avoid light degradation. DTAB/NaSal samples with a surfactant concentration of 12 mM and salt concentration to give constant values of C_{SALT}/C_{DTAB} (=0.42, 0.85, 1.27, 1.69, and 2.54) were prepared by weighing appropriate amounts of surfactant and NaSal and homogenized by mixing and heating to about 60 °C for one hour. Then, these solutions were left standing for one week at the temperature of measurements to reach equilibrium.

Stress-controlled measurements were done in a Carri-Med C-50 rheometer equipped with a cone-and-plate geometry

Table 1
Parameters of the model for the systems and conditions chosen. References where data were taken are also indicated.

System	Surf conc. (wt.%)	Salt/surf	Temp. (°C)	BMP model parameters					Refs.
				φ_0	φ_∞	$\vartheta \times 10^2$	G_0	$k\lambda \times 10^2$	
CPCl/Sal	21.5	0.5	25	0.25	6	20	537	10	[42]
CPCl/Sal	14.6	0.5	25	0.21	6.5	50	281.6	9	[42]
CPCl/Sal	10	0.5	25	0.2	7	75	190	7	[42]
CPCl/Sal	6.3	0.5	25	0.19	7	80	71.3	6	[42]
CPCl/Sal	5.1	0.5	25	0.14	8.5	160	46.01	3.5	[42]
CTAT	3	1	25	0.0105	18.1	0.0001	21.9	4.1	[39]
CTAT	5	1	25	0.027	19.5	0.7	58	2.5	[39]
CTAT	10	1	25	0.006	14.8	0.8	164	0.301	[39]
CTAT	15	1	25	0.005	12.7	1	380	0.105	[39]
CTAT	20	1	25	0.0042	12	1.5	640	0.043	[39]
DTAB/NaSal	0.55	0.42	30	0.05	13.5	80	0.38	17.9	[47]
DTAB/NaSal	0.55	1.27	30	0.3	13	30	0.38	6.8	[47]
DTAB/NaSal	0.55	1.69	30	0.9	15.5	1	0.45	9.6	[47]
DTAB/NaSal	0.55	4.2	30	5.05	76	0	0.45	0.5	[47]
P103	20	1	30	28.98	56.8	0.01	2.33	0.05	[46]
P103	20	1	32	3.83	27.3	0.015	19.43	0.02	[46]
P103	20	1	33	1.43	29.2	0.017	12.21	0.021	[46]
P103	20	1	34	0.35	22.7	0.0097	16.1	0.053	[46]
P103	20	1	35	0.033	39.5	0.11	8.22	0.0357	[46]
P103	20	1	36	0.017	39.8	1	7.13	0.045	[46]

(0.035 radians and 40 mm) and in two parallel plates (25 and 40 mm in diameter) with a gap of 0.2 mm in both cases. Steady simple shear strain-controlled experiments were performed in a TA Instruments Ares-22 rheometer with cone-and-plate geometry of 0.1-radian and 50-mm in diameter. Birefringence measurements were performed in a strain-controlled TA Instruments Ares-22 rheometer coupled to an Optical Analysis Module (OAM2). Parallel quartz glass plates of 38.1 mm in diameter were used. For both rheological and rheo-optics measurements, an environmental control unit was placed around the cone-and-plate fixture to prevent water evaporation. Temperature was controlled within 0.1 °C during measurements.

Nonlinear rheological data as a function of surfactant concentration for micellar solutions of cetylpyridinium chloride–sodium salicylate (CPCl–Sal) in 0.5 M NaCl brine were taken from Berret et al. [42].

4. Results

Fig. 1 depicts the reduced shear stress ($\sum_r$) versus the reduced shear rate ($\dot{\Gamma}_r$) for three micellar solutions: CTAT micellar solutions as a function of surfactant concentration measured at 25 °C (Fig. 1A); 20 wt.% Pluronics in water as a function of temperature (Fig. 1B); and DTAB/NaSal at different DTAB/NaSal ratios measured at 30 °C (Fig. 1C). These systems were chosen because they cover the main variables that affect the shear banding intensity parameter, namely, surfactant concentration, temperature, and surfactant/salt ratio. Fig. 1A shows that the model reproduces the sigmoidal reduced curves, meaning that the bands are still not fully developed as discussed elsewhere [43]. The inset in Fig. 1A shows the same data but represented in the $\sum$ versus $\dot{\Gamma}$ plot. Here, plateaus are drawn corresponding to the developed banding flow on the master dynamic phase diagram. The criterion to locate the plateau is based on the equal minima in the dissipated energy (Eq. (4)) [37,39]. As observed, the dynamic phase diagram is remarkably similar to equilibrium liquid–vapor phase diagrams. However, when the same data are plotted in reduced coordinates, these curves become anti-symmetric around the non equilibrium critical point, akin to the equilibrium ferromagnetic transition [36]. Notice that the stress plateau shrinks as the *necp* is approached and it vanishes at the critical concentration in reduced coordinates (1, 1). The rheological data of the other two micellar systems also yield the master dynamic phase diagram (insets in Fig. 1B and 1C), and are anti-symmetric in reduced coordinates with increasing temperature (Fig. 1B) or varying salt-to-surfactant ratio (Fig. 1C). These results suggest that a non-equilibrium critical point, akin to its equilibrium counterpart, occurs as a thermodynamic variable is varied and that this phenomenon is a general one for micellar solutions in the shear-banding flow regime.

Fig. 2 depicts plots of birefringence ($\Delta n'$) for a 20 wt.% Pluronics P103 measured at different temperatures and at an identical normalized shear rate within the shear banding region. The normalized shear rate was chosen to pass at or near the *necp* as temperature is increased. The dimensionless shear flow curves for the same system at the measurement temperatures as well as the coexistence line and the critical point are depicted in the inset, where the solid lines are the predictions of the model using Eq. (15); the open circles in the inset indicate the dimensionless shear rate at which rheo-optical measurements were performed. For isotherms below the *necp*, $\Delta n'$ exhibits oscillations with large amplitudes (data *d*), indicating that the refractive index changes due to the formation of a second phase induced by shear, inasmuch as measurements were made within the shear banding region. The amplitude and frequency of the birefringence oscillations become even larger as the *necp* is approached, indicating increasingly erratic concentration and structure fluctuations, which are characteristic of near critical behavior (data indicated by *c*). It is noteworthy to remark that a closer approach to the *necp* is extremely difficult in rheological experiments, due to the lack of enough temperature control (<0.01 °C) in existing rheometers. Notice, however, that above the critical point, within the homogeneous flow region, the amplitude of the birefringence oscillations damps out (data *b*) and vanishes as temperature departs from the critical isotherm (data *a*).

Fig. 3 depicts plots of the birefringence variance, $\xi = \sum(\Delta n_i - \langle \Delta n \rangle)^2 / \langle \Delta n \rangle^2$, (being Δn_i the birefringence at a given time *i* and $\langle \Delta n \rangle$ the time-average value) and the normalized dissipated energy ($\widehat{G}$) versus the normalized shear rate for the 20 wt.% Pluronics P103 solution measured at different temperatures. For isotherms outside the shear banding region (far from the *necp*), a minimum is observed (Fig. 3B, curves a and b) and small birefringence fluctuations are detected (Fig. 3A, curve a), indicating the presence of a homogeneous phase. Birefringence fluctuation becomes slightly larger as the shear banding region is approach (Fig. 3B, curve b). Within

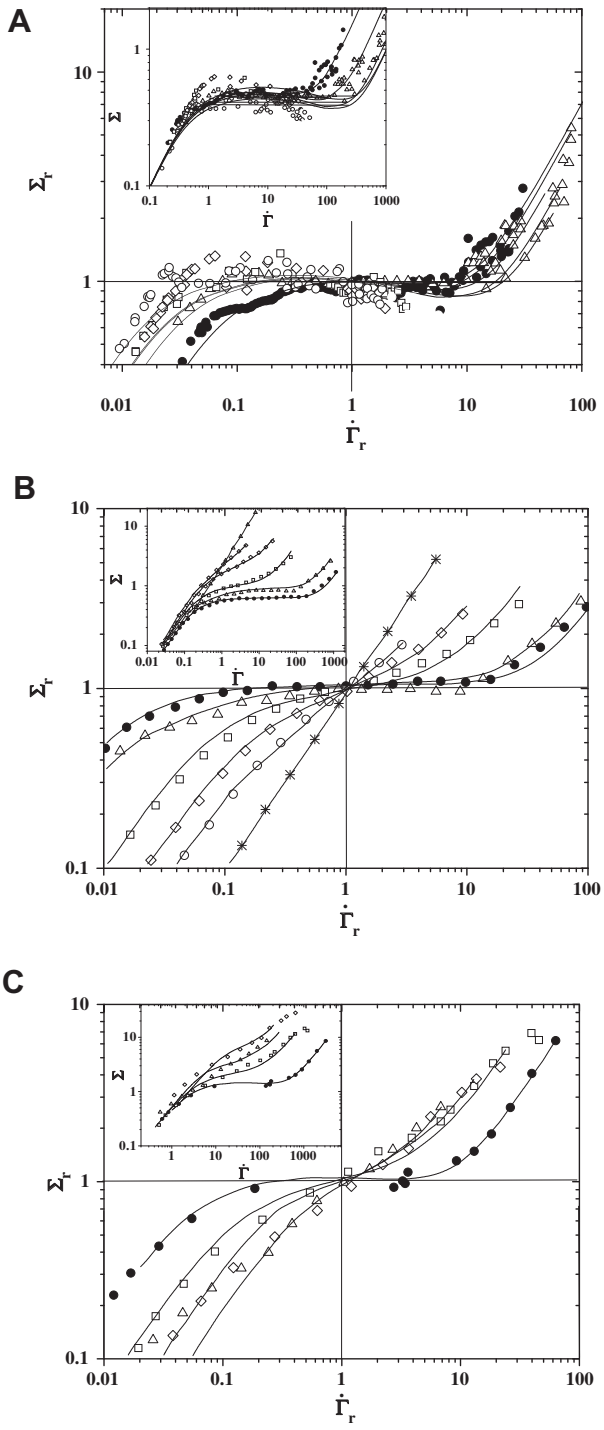

Fig. 1. Reduced shear stress ($\sum_r$) versus the reduced shear rate ($\dot{\Gamma}_r$) for different systems: (A) CTAT micellar solutions as a function of surfactant concentration: (•) 3 wt.%, (△) 5 wt.%, (□) 10 wt.%, (◇) 15 wt.% and (○) 20 wt.%, measured at 25 °C. (B) Pluronics(P103)/water 20 wt.% as function of temperature: (✳) 30 °C, (○) 32 °C, (◇) 33 °C, (□) 34 °C, (△) 35 °C, (•) 36 °C. (C) DTAB/NaSal/water as function of the relationship C_S/C_D: (•) 0.42, (□) 1.27, (◇) 1.69, (△) 4.2; DTAB concentration 5 wt.% and 30 °C. Insets: Berret-like normalization for the same systems. The solid lines represent the best fit of the BMP- Model. The BMP model parameters are in Table 1.

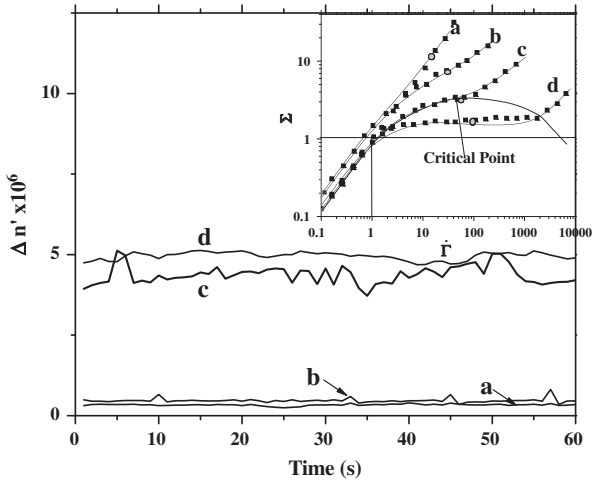

Fig. 2. Birefringence ($\Delta n'$) for a 20 wt.% Pluronics P103/water as function of temperature: (a) 32 °C, (b) 34 °C, (c) 35 °C; (d) 36 °C. Inset: Σ versus $\dot{\Gamma}$ for 20 wt.% Pluronics P103/water as function of temperature.

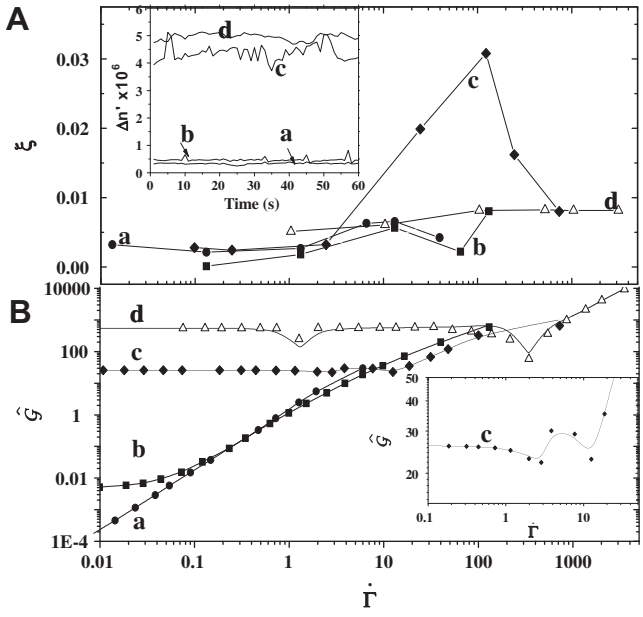

Fig. 3. (A) Birefringence variance, $\xi = \sum(\Delta n_i - <\Delta n>)^2/\langle\Delta n\rangle^2$ and (B) the normalized dissipated energy ($\hat{G}$) versus normalized shear rate measured at different temperatures: (a) 30 °C, (b) 32 °C, (c) 35 °C; (d) 36 °C , respectively. Inset: Birefringence ($\Delta n'$) for a 20 wt.% Pluronics P103/water as function of temperature.

the shear banding region, the emergence of two bands corresponds to a stable regime with high values in birefringence but with small variance (curve d). The dissipated energy, in turn, exhibits two minima with identical depth (Fig. 3B, curve d), which correspond to the normalized shear rates that bound the shear banding region; the minima diminish in depth and become closer as the *necp* is approached. Near the critical point, the dissipated energy exhibits shallow minima (Fig. 3B, curve c); in fact, because the depths of the two minima in curve c (Fig. 3B) are quite shallow, data was amplified near the position of the two minima for clearer observation (inset in Fig. 3B). In this regard, small perturbations in the system may cause strong fluctuations in shear rate (rheo-chaos) in the neighborhood of the *necp*. In summary, once the critical isotherm is surpassed, the oscillations and amplitude of the birefringence damp out and nearly vanish, resulting in small birefringence variance, indicating again the formation of a single homogeneous phase.

To distinguish whether the birefringence signals arise out of stochastic or deterministic processes the main metric and dynamical invariants of the birefringence data, shown in Fig. 2, were calculated. First, the *correlation dimension R*, which provides with an

idea of the geometry of the attractors in phase space in which the birefringence trajectories lie in the asymptotic limit, were calculated. Next, the *Lyapunov exponent* v, which is a measure of the trajectories difference of two neighbors, was calculated. The condition of chaotic dynamics in a system requires that for this correlation integral, $C_R(N, R) > 2$ and $v > 0$. The analysis is done by reconstructing the phase space embedding the experimental time-series of birefringence in m dimensions using time delay vectors L, so that the invariants associated with the dynamics may be calculated unambiguously. The correlation integral of the set $\{x_1, x_2, \ldots, x_N\}$ is given by:

$$C(N,R) = \frac{2}{N(N-1)} \sum_{i,j} H(R - |x_i - x_j|) \text{ with } 1 \leqslant i \leqslant j \leqslant N, \qquad (17)$$

where $H(x)$ is the Heaviside step function [44,45].

An algorithm [46] that computes the Grassberger–Procaccia correlation [47] of an attractor from a finite sample of N experimental points was used. This algorithm measures the distance between all pairs of points of the attractor, but discards distances higher than a cutoff r_0. For small R's, $C_R \approx R^v$, where v, the Lyapunov exponent, gives useful information about the local structure of the attractor [48]. This exponent can be obtained from the plot of $\log C_R$ versus $\log R$ (Fig. 4). A plateau in the plot of $v(m)$ versus $\log R$ gives the correct v for a chosen embedding dimension m. The value of v determines the dynamics type: if $v < 0$, the dynamics is deterministic, if v is positive but smaller than m, deterministic chaotic dynamics is observed, and if $v > m$, the dynamics correspond to random noise [45].

Fig. 4 shows the log of the correlation versus log of the correlation dimension obtained from the dynamical analysis of the birefringence data disclosed in Fig. 2. This figure reveals that v becomes positive at temperatures higher than 34 °C, indicating the onset of chaos at this temperature, followed by a maximum in the Lyapunov exponent at the *necp* (Table 2), and a decreased in v thereafter. The existence of a positive Lyapunov exponent is the footprint of chaotic dynamics. Incidentally, the Lyapunov coefficients were calculated for values of m of 1, 2, 3 and 4, giving in all cases the criterion for deterministic chaos, that is, $0 < v < m$.

Fig. 5 depicts the isothermal flow susceptibility $\kappa_T[= -\dot{\Gamma}^{-1}(d\dot{\Gamma}/d\Sigma)_T]$ of CPCl–Sal in 0.5 M brine micellar solutions at different concentrations versus the reduced shear rate, calculated at different reduced shear rates for the reduced rheological data near the *necp* (not shown). As detailed elsewhere [35], the isothermal flow susceptibility is the non-equilibrium analogous of the isothermal compressibility. This figure discloses that κ_T diminishes

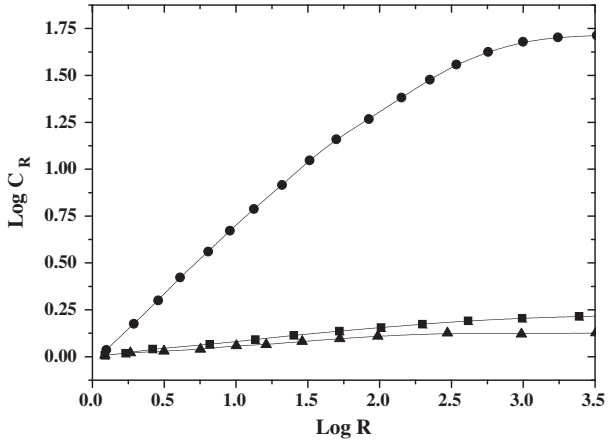

Fig. 4. Log of correlation integral versus log correlation dimension, for a 20 wt.% Pluronics P103/water as function of temperature: (▲) 30 °C, (●) 35 °C, (■) 36 °C.

Table 2
Lyapunov exponents calculated for the micellar systems for various conditions of surfactant concentration, temperature and salt /surfactant weight ratio.

CTAT micellar solution				
Surfactant concentration (wt.%)	3	5	10	15
Lyapunov exponent	0.001	1.22	0.22	0.17
Pluronics(P103)/water (20 wt.%)				
Temperature	30	32	35	36
Lyapunov exponent	0.001	0.007	0.48	0.12
DTAB/NaSal/water				
Relationship C_S/C_D	0.42	1.27	1.69	4.2
Lyapunov exponent	0.8	0.046	0.094	0.01907

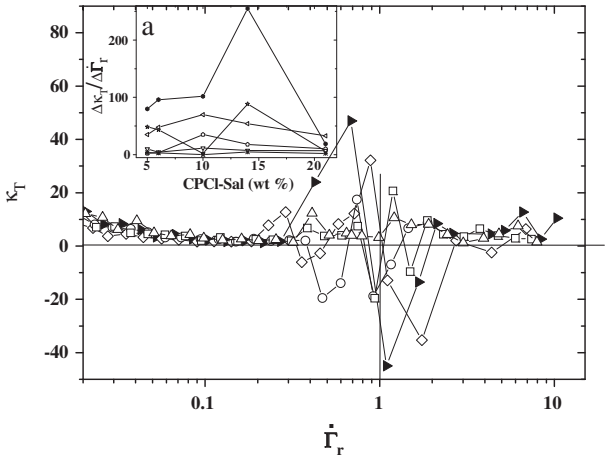

Fig. 5. Isothermal flow susceptibility versus the normalized shear-banding intensity parameter as function of surfactant salt relationships: (□) 5 wt.%, (○) 6 wt.%, (◇) 10 wt.%, (►) 14 wt.%, (△) 21 wt.% for a CPCL–Sal in 0.5 M brine solution measured at 25 °C. Inset: $|\Delta K_T|/|\Delta\dot{\Gamma}|$ versus CPCl–Sal concentration as function of reduced shear rate. The lines are aid-eye. The Lyapunov exponents are in Table 2.

monotonically with reduced shear rate for $\dot{\Gamma} < \dot{\Gamma}_r$; however, at shear rates within the shear banding region, κ_T fluctuates from positive to negative values, which become larger as surfactant concentration increases at $\dot{\Gamma}_r \approx 1$ (i.e., at the surfactant concentration where the *necp* occurs) and leads to the divergence of κ_T. At shear rates larger than that at which the shear banding region ends, κ_T again becomes small, positive and nearly independent on surfactant concentration. The inset of Fig. 4 shows the absolute κ_T-fluctuations with respect to the dimensionless shear rate, $|\Delta\kappa_T|/|\Delta\dot{\Gamma}|$, versus CPCl-Sal concentration. For concentrations close to the *necp*, $|\Delta\kappa_T|/|\Delta\dot{\Gamma}|$ grows substantially, and near $\dot{\Gamma}_r \approx 1$, it diverges. Notice that this behavior is similar to that observed for its equilibrium counterpart, the isothermal compressibility, which diverges in the neighborhood of the equilibrium critical point.

Fig. 6 depicts data on the experimental coexistence curve $(\Delta\dot{\Gamma} = \dot{\Gamma}_{c1} - \dot{\Gamma}_{c2})$ versus ϑ in log–log plot for various micellar systems examined here. This figure reveals that the width of the reduced coexistence curve $(\dot{\Gamma}_{c1} - \dot{\Gamma}_{c2})$ diminishes as ϑ decreases, and near the critical point $\dot{\Gamma}_{c1} - \dot{\Gamma}_{c2}$ diminishes more rapidly toward zero at the *necp*, as expected. Inasmuch as only a few data points were available in this temperature (ϑ) range, the limiting slope predictions of the BMP model, included as a dashed line, pass in the vicinity of the data points. According to results presented elsewhere [35], the critical exponent for the coexistence region (β) is 5.7; from the experimental data shown in the limiting slope, taking the average of all data points near the *necp*, the experimental critical exponent β is 5.0 ± 0.5.

Fig. 7 shows the normalized power dissipation under shear banding flow $C_{\sigma_r} = \frac{G_0\varphi}{N}\left(\frac{\partial\sigma_r\dot{\gamma}_r}{\partial\vartheta}\right)_\sigma$ against ϑ in log–log plot for the

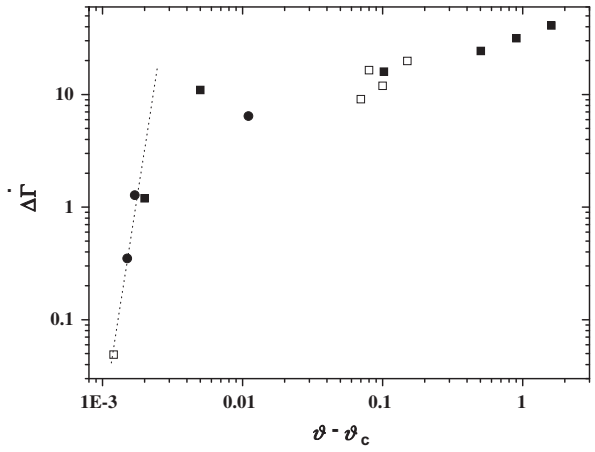

Fig. 6. Difference of normalized critical shear rates versus the normalized shear-banding intensity parameter for (■) CPCL–Sal in 0.5 M brine solution measured at 25 °C, (•) CTAT solutions measured at 25 °C, (□) Pluronics(P103)/water 20 wt.%.

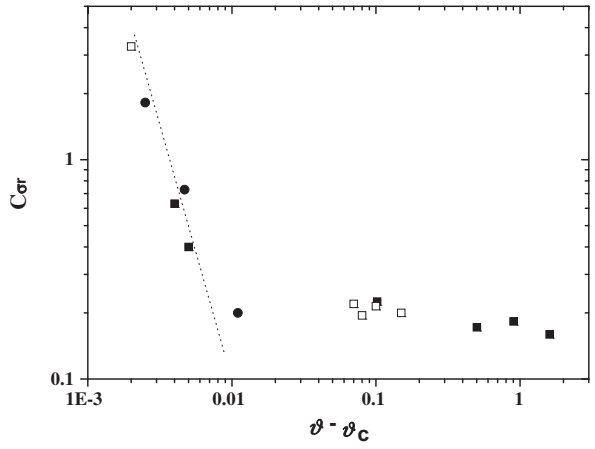

Fig. 7. Normalized power dissipation under shear-banding flow versus the normalized shear-banding intensity parameter for a (■) CPCL–Sal in 0.5 M brine solution measured at 25 °C, (•) CTAT solutions measured at 25 °C, (□) Pluronics(P103)/water 20 wt.%.

various micellar systems examined here. The data depicts that C_{σ_r} increases slowly with decreasing ϑ and then more rapidly as $\vartheta \to \vartheta_c$. Evidently, C_{σ_r} diverges as the *necp* is approached; incidentally, C_{σ_r} also exhibits strong fluctuations that increase rapidly as the *necp* is reached (not shown). Again due to the lack of enough data closer to the *necp*, the limiting slope predictions of the model, included as a dashed line, pass over the available data in this region. The critical exponent α predicted by the BMP model for $C\sigma_r$ is 2.2 [35]; from the experimental data shown in the limiting slope, taking the average of all data points closer to the *necp*, the experimental value of α is 1.8 ± 0.5.

A similar analysis for the isothermal flow susceptibility κ_T (not shown) indicates that this function diverges as $\vartheta \to \vartheta_c$ with a critical exponent, ϑ, around 7.4 ± 3.2, which is smaller than to the one predicted by the BMP model (ϑ = 11.5). It is noteworthy that both $\dot{\Gamma}_{c1} - \dot{\Gamma}_{c2}$ and $C_{\sigma r}$ (Figs. 5 and 6) are predicted well by the model, although the few points of experimental data cannot enable an accurate determination of the slope assigned to the critical exponents. For the case of ϑ, however, the experimental error may be larger due to the rapid divergence of κ_T (the predicted value of the this critical exponent is 11.5) and the small amount of data near the *necp*.

5. Discussion and conclusions

Experimental rheological and rheo-optical evidences of the existence of a non- equilibrium critical point induced by shear flow are presented here. Four different micellar solutions were selected since the chosen thermodynamic variables (temperature, surfactant concentration or salt/surfactant ratio) are easy to control near the *necp*. In addition, these thermodynamic variables are included in the BMP model through the shear banding intensity parameter.

The experimental shear flow curve plotted in normalized shear stress and shear rate ($\sum$ versus $\dot{\Gamma}$) is remarkably similar to the equilibrium liquid–gas phase transition: both have a coexistence region, a spinodal region, two metastable regions, and a critical point. In fact, when the temperature or the surfactant concentration is increased, the shear banding flow region (coexistence region) shrinks and disappears at a "critical" temperature or surfactant concentration, defining a "critical" line (or surface when an extra component such as a salt is added), because polymer-like micellar solutions are at least two-component systems. In addition, due to the flow-concentration coupling, the regions of instability broaden to include regions of positive slope in the constitutive flow curve [49]. Consequently, the experimental critical point shifts downwards in temperature or surfactant concentration. In fact, rheo-optical data reveal large fluctuations and increasingly erratic oscillations of the flow birefringence as the *necp* is approached. This is related to the flattening of the dissipated energy per unit time as the *necp* is approximated and so, small variations in the control thermodynamic variable produce large fluctuations and oscillations in the vicinity of the critical point. The Lyapunov analysis of the birefringence data (Fig. 2) reveals that the shear banding undergoes a transition from deterministic dynamics to a chaotic one as temperature approaches the critical one. The Lyapunov exponents which are positive but smaller than the embedding dimension, go through a maximum near the *necp*, indicating unambiguously that the chaos becomes larger as this critical point is approached. In fact, other variables such as the difference of critical shear rates (analogous of the critical isotherm), the isothermal flow susceptibility (analogous of isothermal compressibility) and the heat flow dissipation capacity (analogous to the heat capacity) also exhibit large fluctuations in the neighborhood of the critical point. This may be a consequence in part due to the coupling of flow and concentration, which also produces oscillations, long transient in flow inception and rheo-chaos in the shear banding flow region. The BMP model reproduces quite well the master flow phase diagrams and the anti-symmetric reduced flow curves. Unfortunately, it is not possible to determine accurately the critical exponents due to the small amount of experimental data, which diminishes the accuracy in the numerical estimation of the slope of the plots shown (Figs. 5 and 6). However, the model's estimates obtained from plots shown in Figs. 5 and 6 as solid lines (and dashed lines in the insets) suggest that the values of the critical exponents are larger than their counterpart equilibrium ones and similar to the values predicted by the BMP model [35]. This indicates that flow accelerates the divergence of the extended thermodynamic parameters (κ_T and C_{σ_r}) because the approach to the *necp* is faster than in equilibrium systems, giving as a result lower critical points in flow systems. Finally, it is noteworthy that predictions of the extended BMP model with regard to the sigmoidal flow curve are in agreement with those of the GENERIC formalism [50].

Acknowledgement

We acknowledge the financial support, Project 100195, from the National Council of Science and Technology (CONACYT).

References

[1] J.-F. Berret, Molecular gels, in: R.G. Weiss, P. Terech (Eds.), Materials with Self-Assembled Fibrillar Networks. Springer, Secaucus, 2006, pp. 677–720.
[2] J.E. Puig, F. Bautista, J.F.A. Soltero, O. Manero, in: R. Zana, E.W. Kaler (Eds.), Giant Micelles: Properties and Applications, Francis and Taylor, New York, 2007, pp. 289–322. Chap. 9.
[3] J.I. Escalante, H. Hoffmann, Rheol. Acta 39 (2000) 209.
[4] J.-F. Berret, Séréro, Y. Phys. Rev. Lett. 87 (2001) 048303–048307.
[5] K. Krishnan, B. Chapman, F.S. Bates, T.P. Lodge, K. Almadal, W. Burghardt, J. Rheol. (46) (2002) 529–554.
[6] J.F.A. Soltero, F. Bautista, J.E. Puig, O. Manero, Langmuir 15 (1999) 1604.
[7] J.-F. Berret, Langmuir 13 (1997) 2227.
[8] M.E. Cates, T.C.B. McLeish, G. Marucci, Europhys. Lett. 21 (1993) 451.
[9] P.T. Callaghan, M.E. Cates, C.F. Rofe, J.B.F.A. Smoulders, J. Phys. II 6 (1996) 375.
[10] R. Makhloufi, J.-P. Decruppe, A. Aït-Ali, R. Cresseley, Europhys. Lett. 32 (1995) 253.
[11] C. Grand, J. Arrault, M.E. Cates, J. Phys. II 7 (1996) 1071.
[12] P. Fischer, H. Rehage, Rheol. Acta 36 (1997) 13.
[13] A. Aït-Ali, R. Makhloufi, J. Rheol. 41 (1997) 307.
[14] J.-P. Decruppe, E. Cappelaere, R. Cresseley, J. Phys. II 7 (1997) 257.
[15] J.-F. Berret, G. Porte, Phys. Rev. E 60 (1999) 4268.
[16] R. Mair, P.T. Callaghan, Europhys. Lett. 36 (1996) 719.
[17] J.-F. Berret, D.C. Roux, P. Lindner, Eur. Phys. J. B 5 (1998) 67.
[18] J.-P. Decruppe, S. Lerouge, J.-F. Berret, Phys. Rev. E 63 (2001) 0225011.
[19] Y.T. Hu, A. Lips, J. Rheol. 49 (2005) 1001.
[20] G.H. McKinley, W.P. Raiford, R.A. Brown, R.C. Armstrong, J. Fluid Mech. 223 (1991) 411.
[21] J.A. Byars, A. Oztekin, R.A. Brown, G.H. McKinley, J. Fluid Mech. 271 (1994) 173.
[22] N.A. Spenley, X.F. Yuan, M.E. Cates, J. Phys. II Fr. 7 (1996) 1071.
[23] P. Español, X.F. Yuan, R.C. Ball, J. Non-Newtonian Fluid Mech. 65 (1996) 93.
[24] F. Greco, R.C. Ball, J. Non-Newtonian Fluid Mech. 69 (1997) 195.
[25] J.-F. Berret, G. Porte, J.P. Decruppe, Phys. Rev. E 55 (1997) 1668.
[26] J.K.G. Dhont, W.J. Briels, Rheol. Acta 47 (2008) 257.
[27] T.C.B. Mc. Leish, R.C. Ball, J. Polym. Sci. 24 (1986) 1735.
[28] A. Onuki, K. Kawasaki, Ann. Phys. (NY) 121 (1979) 456.
[29] D. Thirumalai, J. Chem. Phys. 84 (1987) 5869.
[30] S.D. Lee, J. Chem. Phys. 86 (1987) 6567.
[31] S.Q. Wang, W. Gelbart, J. Phys. Chem. 90 (1989) 597.
[32] P.D. Olmsted, P. Goldbart, Phys. Rev. A 41 (1990) 4578.
[33] P.D. Olmsted, P. Goldbart, Phys. Rev. A 46 (1992) 4966.
[34] O. Manero, F. Bautista, J.H. Pérez-López, J.E. Puig, J. Non-Newtonian Fluid Mechs. 146 (2007) 22.
[35] F. Bautista, M. Muñoz, J. Castillo-Tejas, J.H. Pérez-López, J.E. Puig, O. Manero, J. Phys. Chem. B 113 (2009) 16101.
[36] J.J. Binney, N.J. Dowrick, A.J. Fischer, M.E.J. Newman, The Theory of Critical Phenomena. An Introduction to the Renormalization Group. Clarendon Press, Oxford, 1993.
[37] F. Bautista, J.H. Pérez-López, J.P. García, J.E. Puig, O. Manero, J. Non-Newtonian Fluid Mechs. 144 (2007) 160.
[38] F. Bautista, J.M. de Santos, J.E. Puig, O. Manero, J. Non-Newtonian Fluid Mechs. 80 (1999) 93.
[39] F. Bautista, J.F.A. Soltero, E.R. Macías, J.E. Puig, O. Manero, J. Phys. Chem. B 106 (2002) 13018.
[40] S.Z. Hess, Physica A 87A (1997) 273.
[41] J.K.G. Dhont, Phys. Rev. E 60 (1999) 4534.
[42] J.-F. Berret, D.C. Roux, G. Porte, J. Phys. II Fr. 4 (1994) 1261;
J.-F. Berret, J. Appell, G. Porte, Langmuir 9 (1999) 2851.
[43] M.E. Cates, S. Fielding, in: R. Zana, E.W. Kaler (Eds.), Giant Micelles: Properties and Applications, Francis and Taylor, New York, 2007 (Chapter 9).
[44] N.H. Packard, J.P. Crutchfield, J.D. Farmer, R.S. Shaw, Phys. Rev. Lett. 45 (1980) 712.
[45] F. Takens, in: B.L.J. Braakma et al. (Eds.), Dynamical Systems and Bifurcations, Lecture Notes in Math., vol. 1126, Springer, Heilderberg, 1985.
[46] Theiler, J. Phys. Rev. A 36 (1987) 4456.
[47] P. Grassberger, I. Procaccia, Phys. Rev. Lett. 50 (1983) 346.
[48] R. Bandyopadhyay, G. Basappa, K.S. Sood, Phys. Rev. Lett. 84 (2000) 2022.
[49] B. García-Rojas, F. Bautista, J.E. Puig, O. Manero, Phys. Rev. E 60 (3) (2009) 036313.
[50] M. Grmela, F. Chinesta, A. Ammar, Rheol. Acta 49 (2010) 495.